ACS OMEGA

http://pubs.acs.org/journal/acsodf

Article

Performance Evaluation of Composite Antisalt Agents and the Antisalt Dynamics Simulation Mechanism

Chao Ma,* Yan Chen, Wen dong Ren, Xing yu Liu, Wen Gu, and Hui li Zhou

Cite This: *ACS Omega* 2022, 7, 13075−13082

Read Online

ACCESS | Metrics & More | Article Recommendations

ABSTRACT: The conventional ferrocyanide complex ($[Fe(CN)_6]^{4-}$) has been widely used as a scale inhibitor under mild conditions, but its oxidation at high temperature compromises the subsequent wastewater treatment processes. To conquer the inadequacies of $Fe(CN)_6]^{4-}$, aminotriacetamide (NTA) was synthesized using chloroacetic acid as an initial material and its molecular structure was characterized using FT-IR spectroscopy, H-NMR, and TGA. NTA was exploited in combination with polyaspartic acid (PASP) and sodium dodecyl benzene sulfonate (SDBS) to prepare a high-performance antisalt composite, and the scaling inhibitor performance was evaluated. The results revealed that as the concentration of the antisalt composite increased from 0.5 to 1.2 wt %, the solubility and inhibition rate increased by 95.6 and 12.33%, respectively, at 100 °C. The results from molecular simulation evidenced that the order of binding energy between a unit mass of the salt inhibitor and sodium chloride crystal increased in the following order; SDBS > NTA > PASP. The deformation strength between the salt inhibitor and sodium chloride crystal increased as follows: NTA > PASP > SDBS. In addition, the antisalt composite mainly hampered salt precipitation through strong adsorptions arising from both the nitrogen atom of NTA and oxygen atom of SDBS with the sodium atom of sodium chloride crystals, and as a result, it not only altered the crystalline form of sodium chloride but also reduced the adsorption of sodium atoms and eventually improved the salt solubility.

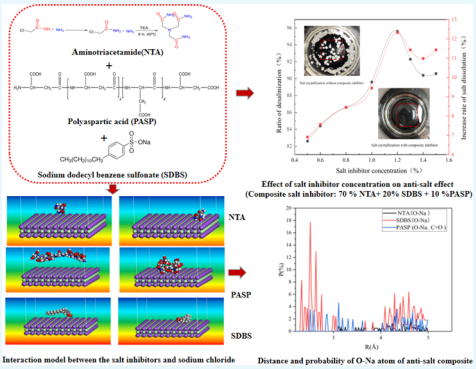

1. INTRODUCTION

In the oil and gas production processes, a huge volume of water is injected into a reservoir to sustain the reservoir pressures at desired levels, whereby there is a possibility of scale formation, consequently obstructing the reservoir and eventually causing formation damages.[1] The deposition of scale minerals in the process of hydrocarbon production has long been a concern in petroleum industries. As examples, Pineywoods oilfield, Rotllegende gas field, and Beihai Brage oilfield have been facing serious issues from scale deposits.[2] In China, most of the oilfields are currently in the middle and late stages of exploitation and the oilfields with serious scale deposits are mainly concentrated in the Jianghan oilfield, Zhongyuan oilfield, and Southwest oilfield.[3−7] This issue leads to adverse phenomena including pipeline obstruction, increased rate of corrosion, and reservoir damage, which negatively impact the normal production of oilfields, and eventually cause tremendous economic losses.[8−11] Moreover, in some gas wells in the central and eastern Sichuan oil and gas fields of Southwest oilfield, natural gas carries high saline water into the gas transmission line. Consequently, as the pressure and temperature vary, the scale mineral precipitation results in the reduction of the gas well transmission pressure and ultimately influences the downstream gas consumption.[12]

Based on the theoretical understanding of the salt formation mechanism in oil and gas wells, a vast number of technologies have been developed to mitigate their depositions, among which chemical methods based on scale inhibitors are used. Scale inhibitors are more effective in controlling the precipitation of salts because of their attractive cost and possibility of effectively expanding the salt formation cycle.[13−15] Considered as the most commonly used scale inhibitor in oil and gas industries, the ferrocyanide complex ($[Fe(CN)_6]^{4-}$) not only significantly improves the solubility of sodium chloride but also alters the morphology of salt crystals. Moreover, $[Fe(CN)_6]^{4-}$ in an aqueous solution exhibits a stronger affinity with sodium ions, as a result forming a stable chelate which tremendously reduces the migration of sodium ions toward chloride ions and ultimately improving the solubility of sodium chloride.[16] However, as the temperature rises above 70 °C, $[Fe(CN)_6]^{4-}$ readily loses the water crystal.

Received: January 22, 2022
Accepted: March 30, 2022
Published: April 7, 2022

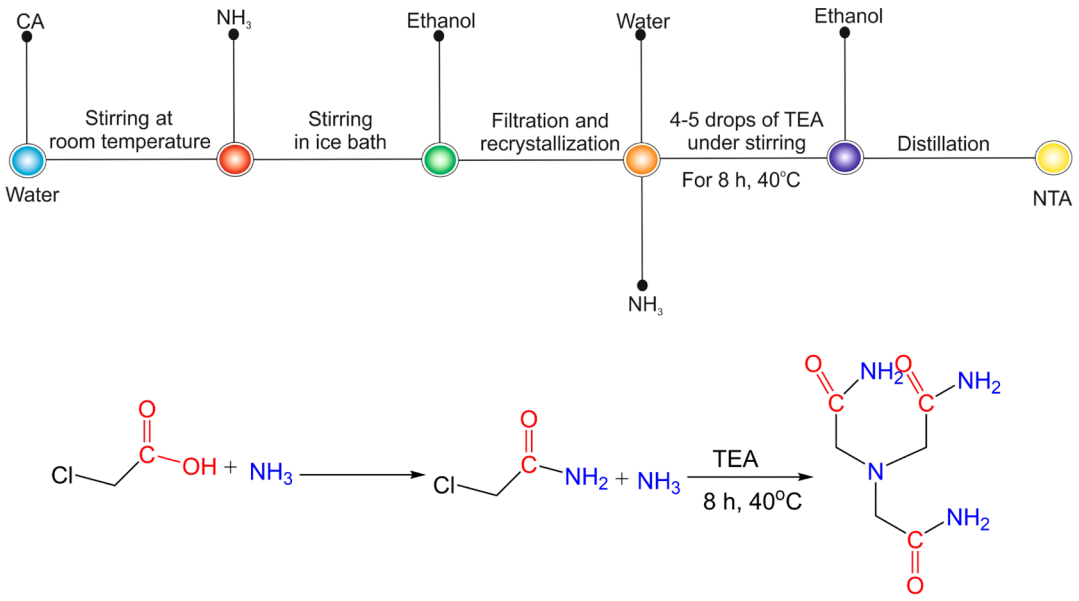

Figure 1. Schematic diagram of the synthesis of NTA.

Having in mind that the temperature of formation containing high-salinity levels generally exceeds 70 °C, the performance of $[Fe(CN)_6]^{4-}$ would be adversely compromised with respect to the inhibition effect. Moreover, $[Fe(CN)_6]^{4-}$ is susceptible to oxidation and even reacts with iron ions to produce Prussian blue color, leading to the discoloration of the inhibiting solution and as a result jeopardizing the subsequent wastewater treatment process. Additionally, the current synthetic strategy for $[Fe(CN)_6]^{4-}$ is complex and cost-attractive. Consequently, these demerits may impede the large-scale manufacturing of $[Fe(CN)_6]^{4-}$ and acceptance in oil and gas industries that always desire high-performance products at a fairly low cost.[17,18] Contrary to $[Fe(CN)_6]^{4-}$, aminotriacetamide (NTA) is well known to exhibit not only certain thermal stability but also an inhibiting effect with respect to sodium, calcium, and magnesium deposits. However, the reports based on the preparation strategy of NTA are scanty within the published literature.

In this work, NTA was prepared using chloroacetic acid (CA) as an initial material. Subsequently, polyaspartic acid (PASP) and sodium dodecyl benzene sulfonate (SDBS) were used as the salt inhibitors in combination with NTA to formulate a high-performance antisalt composite. The performance of the antisalt composite was examined with respect to the inhibiting effect under high geothermal conditions. Moreover, Materials Studio 5.0 molecular simulation software was used to clarify the distinctive antisalt inhibition mechanism with respect to NTA, PASP, and SDBS from the perspective of kinetics. Overall, this work provides a novel avenue for theoretical guidance of the development of antisalt agents to efficiently control scale formation in petroleum industries.

2. EXPERIMENTAL SECTION

2.1. Materials. CA (99.9%), triethylamine (TEA, 99.9%), and ammonia (NH_3, 40.9%) were obtained from Beijing Bailingwei Technology Co. Ltd. Anhydrous ethanol (99.7%) and sodium dodecylbenzene sulfonate (SDBS, 99.8%) were purchased from Tianjin Fu Chen Chemical Reagent Factory. Industrially produced PASP was procured from Shandong Taihe Water Treatment Technology Co. Ltd.

2.2. Synthesis of NTA. The synthesis of NTA was conducted according to a two-step reaction, as illustrated in Figure 1. First, 4.91 g of CA was dissolved in a certain amount of deionized water and the mixture was added into a three-necked flask, followed by the addition of 2 mL of NH_3 under constant stirring in an ice bath for 1 h. Afterward, the formed chloroacetamide was recovered by filtration, followed by recrystallization using anhydrous ethanol. Second, 13.43 g of chloroacetamide was completely dissolved in deionized water and a certain amount of NH_3 was introduced, followed by the addition of 4−5 drops of TEA under constant stirring at 40 °C for 8 h. Once the reaction terminated, the residues were removed by reduced pressure distillation, followed by repeated washing and reduced pressure distillation, dried overnight in an oven to obtain whitish crystals of NTA.

2.3. Characterization. The Fourier transform infrared (FT-IR) spectra were recorded using a Nicolet 560 FT-IR analyzer in the frequency range of 4000−400 cm^{-1}. The H-NMR spectra were recorded using an AVANCE AV 400 analyzer with deuterated chloroform as a solvent. Thermogravimetry analysis (TGA) was performed using a Dupont SDTQ600 thermogravimetry analyzer at a heating rate of 20 °C/min from room temperature to 600 °C under a N_2 atmosphere. A DSC-350L differential scanning calorimeter was employed to examine the thermal stability at a temperature of 25−320 °C and a heating rate of 10 °C/min at a N_2 flow rate of 100 mL/min. An OLYMPUSCX41 biological microscope was used for the microscopic observation of water appearance before and after the addition of the salt inhibitor.

2.3.3. Antisalt Composite Inhibition Test. Solid NTA, liquid sodium dodecylbenzene sulfonate (SDBS), and liquid PASP were mixed in a mass ratio of 7:2:1 and stirred until complete dissolution of NTA to acquire the antisalt composite. The performance of the antisalt composite was examined in 500 mL of saturated brine, and the results were compared with those of saturated brine without the antisalt composite at ambient temperature. Two *U*-shaped hollow metal iron pipes were weighed, and the weights of the watch glass were taken as m_1 and m_2. Subsequently, one end of the latex tube was connected to the *U*-shaped hollow metal, while the other end

https://doi.org/10.1021/acsomega.2c00452
ACS Omega 2022, 7, 13075−13082

was attached to a pipe to allow water circulation. The two *U*-shaped hollow tubes were placed into the above saturated brines and heated until the volume of water reduced to 400 mL. Afterward, the two *U*-shaped hollow metal iron pipes and watch glasses were recorded as m_3 and m_4, respectively. The rate of the antisalt was calculated using the mathematical expression given in eq 1

$$P = \frac{(m_4 - m_2) - (m_3 - m_1)}{m_4 - m_2} \times 100 \quad (1)$$

where P is the rate of the antisalt in %, m_1 is the weight of the *U*-shaped hollow tube in saturated brine containing the antisalt composite in grams, m_2 is the weight of the *U*-shaped hollow tube in saturated brine without the antisalt composite, m_3 is the weight of the *U*-shaped hollow tube and mass of crystallized salt in saturated brine containing the antisalt composite in grams, and m_4 is the weight of the *U*-shaped hollow tube and weight of crystallized salt in saturated brine without the antisalt composite in grams.

2.3.4. Dissolution Rate of the Antisalt Composite. The dissolution rate of the antisalt composite was assessed by dissolving both 1.9 g of the solid antisalt unblocking agent and 0.1 g of the liquid antisalt unblocking agent into 200 mL of deionized water contained in the first flask. 90 g of sodium chloride was added to the mixture and heated to boil in an electric furnace. Subsequently, 1 mL of the supernatant was collected from the sample and transferred into a conical flask, followed by the addition of distilled water. Afterward, 1∼3 drops of a 5% potassium chromate indicator were then introduced, followed by titration with the standard silver nitrate solution. The mixture in the second flask was prepared under identical conditions as mentioned before, except the addition of the antisalt unblocking agent. The dissolution rate of the antisalt composite was calculated according to the following formula 2.

$$H = \frac{V_2 - V_1}{V_1} \times 100 \quad (2)$$

where H is the dissolution rate in %, V_2 is the consumption volume of the silver nitrate solution in the presence of the antisalt composite in milliliters, and V_1 is the consumption volume of the silver nitrate solution without the antisalt composite in milliliters.

2.3.5. Establishment of the Sodium Chloride Crystal Model. As shown in Figure 2a, the sodium chloride crystal model introduced from the imported file had a section of −1,0,0 through cleave surface in the Build Surface tool with the crystal thickness set to 2.0, and the supercell (10 × 10) was established in the Symmetry tool. Moreover, the vacuum layer was established by the Build Vacuum in Crystals tool (vacuum layer thickness was 50), and the sodium chloride crystal model was obtained, as shown in Figure 2b. In addition, both the Forcite module and COMPASS force field were employed to calculate the energy. The surface energy of the sodium chloride crystal cell was $E_{surface}$ = 0 KJ/mol.

2.3.6. Model Establishment of the Antisalt Composite. The molecular models of NTA (see Figure 3a), SDBS (see Figure 3b), and PASP (see Figure 3c) were established using a three-dimensional (3D) atomistic document, and their structures were optimized from three distinct aspects including

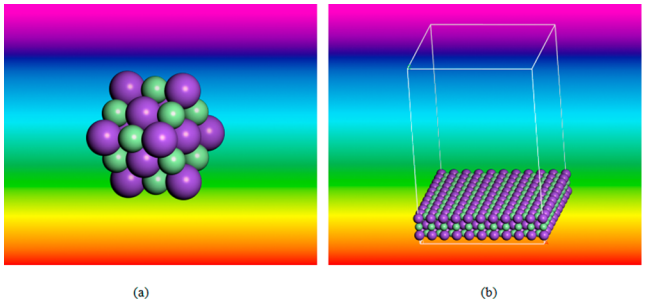

Figure 2. Establishment of the sodium chloride crystal model: (a) sodium chloride structure and (b) established sodium chloride model with a vacuum layer.

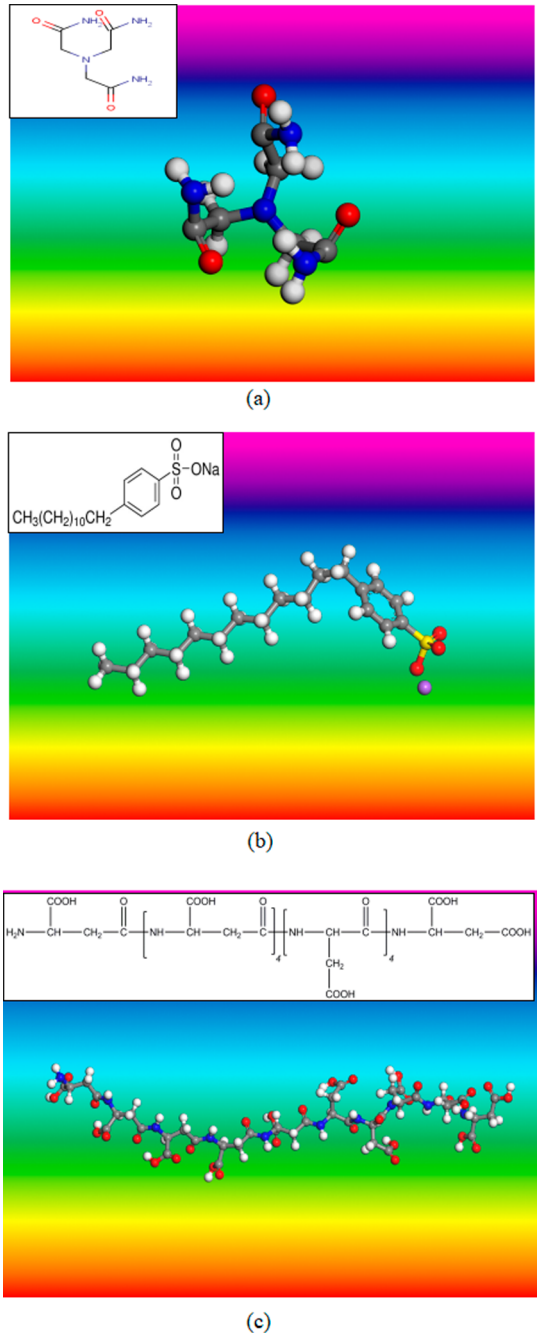

Figure 3. Structure modeling of three scale inhibitors: (a) NTA, (b) SDBS, and (c) PASP (m = 4, n = 4) inhibitors.

https://doi.org/10.1021/acsomega.2c00452
ACS Omega 2022, 7, 13075−13082

energy, geometry optimization, and dynamics under the Forcite calculation module to ensure consistency in the molecular structure, and the performance of the antisalt composite was close to the expected one. Based on spatial structure optimization, the smart algorithm was adopted, and the number of steps was set to 2000. The charge of nitrogen atoms on the NTA amide group obtained by force field assignment was −0.925 C, and the charge of the central nitrogen atom was −0.561 C. The bonding angle between the central nitrogen atom and the adjacent carbon atom was 114°. The structure was basically consistent as per the previous report.[19] By using the Forcite module and COMPASS force field, the initial molecular energies were calculated. Subsequently, the initial molecular energy of the three antisalt agents was acquired as E_{iPASP} = −356.5 KJ/mol, E_{ISDBS} = −49.5 KJ/mol, and E_{INTA} = 68.9 KJ/mol.

2.3.7. Simulation of Binding Energy between Sodium Chloride and the Salt Inhibition System. As shown earlier in Figure 2b, the sodium chloride crystal model was first established, followed by the modification of the constraint tool by selecting fixed atoms to immobilize the sodium chloride crystal. The Forcite analysis tool was used to calculate the $E_{total\ energy}$ and $E_{binding\ energy}$ in the *NVT* system at a temperature of 298 K with a charge assigned by a force field using Ewald's method at a truncation distance of 14. As the molecular weights of the three salt inhibitors constituting the antisalt composite were significantly distinct, the comparison between the binding energies would be ambiguous. The interaction energy per unit mole was therefore converted into the interaction energy per unit weight, and the binding energy per unit weight was then converted to enable realistic comparison.

$$E_{binding\ energy} = E_{total\ energy} - E_{free\ energy} - E_{surface\ energy};$$

$$EM_{binding\ energy} = E_{binding\ energy}/M \quad (3)$$

where $E_{total\ energy}$—salt inhibitor and crystal total energy, kcal/mol; $E_{free\ energy}$—molecular energy of the salt inhibitor, kcal/mol; $E_{surface\ energy}$—total energy of the sodium chloride cell surface (fixed energy is 0), kcal/mol; $E_{binding\ energy}$—energy released after the interaction between sodium chloride and the salt inhibitor, kcal/mol; M—molecular weight of the salt inhibitor, g/mol; and $EM_{binding\ energy}$—energy released by the interaction of sodium chloride and the unit mass salt inhibitor, kcal/g.

2.3.8. Deformation Energy and Radial Function Dynamics Simulation of the Antisalt Composite. The 3D atomistic document was employed to process the established sodium chloride crystal model represented in Figure 2b, and the respective images resulting from the interactions with NTA, SDBS, and PASP in the established sodium chloride cell were introduced into the sodium chloride crystal model, as indicated in Figure 4. Subsequently, the COMPASS force field was further employed using the Badersen temperature control method. Moreover, the *NVT* system was employed using Ewald's method at a truncation distance of 14 at 298 K. Additionally, the Forcite analysis tool was used to calculate the total energy. The established NTA, SDBS, and PASP were in the sodium chloride cell. Finally, the "edit set" tool was used to select the "O" and "N" atoms in NTA, the "O" atom in SDBS, and the "O" and "N" atoms in PASP. Under the Forcite

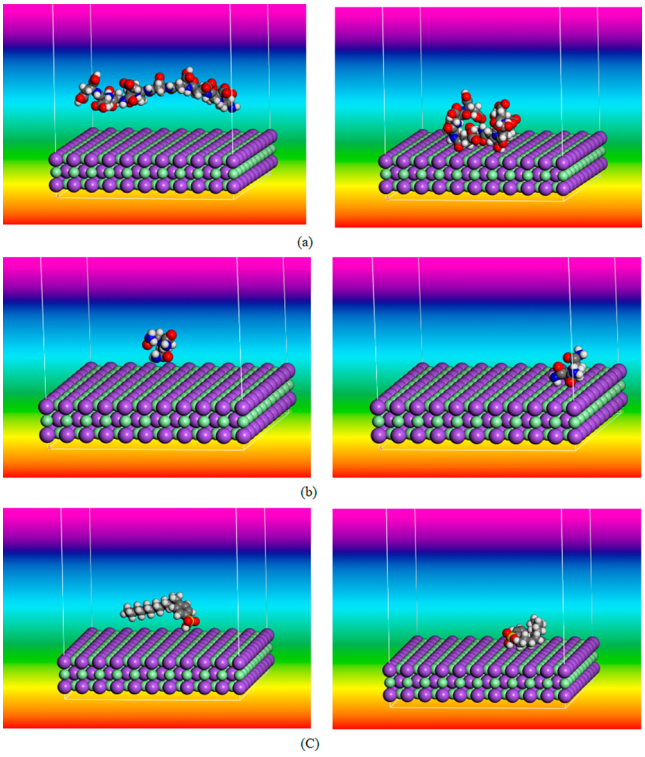

Figure 4. Interaction model between the salt inhibitors and sodium chloride: (a) PASP and sodium chloride, (b) NTA and sodium chloride, and (c) SDBS and sodium chloride.

calculation module, the radial function between the selected atom and the "Na" in the sodium chloride crystal was calculated, and the radial functions between the acting atom and the "Na" in the salt inhibitors were obtained, namely, the distribution probability between the distance of the acting atom and the Na atom in the salt inhibitor. The larger the deformation energy of the salt inhibitor, the greater the change in the spatial configuration during inhibition of salt crystallization, as well as adsorption onto the surface of the salt crystal. This is also an indication of the poor stability of molecular spatial configuration of the salt inhibitor.[20,21] Identically, the interaction energy of a unit mole and deformation energy were converted into unit mass.

$$E_{deformation} = (E_{adsorption\ energy} - E_{free\ energy})$$

$$EM_{deformation} = E_{deformation}/M$$

where $E_{deformation\ energy}$ is the deformation energy generated by the salt inhibitor molecule, kcal/mol; $E_{adsorption\ energy}$ is the energy for the interaction between sodium chloride and salt (the last output structure), kcal/mol; $E_{free\ energy}$ is the total energy for salt inhibitors, kcal/mol; M is the molecular weight of the salt inhibitors, g/mol; and $EM_{deformation}$ is the energy released from the interaction of sodium chloride salt and the unit mass salt inhibitor, kcal/g.

3. RESULTS AND DISCUSSION

3.1. Structural Characterization of the Scale Inhibitors. *3.1.1. IR and NMR Characterization of NTA.* Figure 5 shows the FT-IR spectra of ammonia triacetamide. The large band recorded at 3143 cm^{-1} was ascribed to the stretching vibration of N−H in amide. The stretching vibration of C═O in amide was attributed to the peak at 1729 cm^{-1}. The peaks

https://doi.org/10.1021/acsomega.2c00452
ACS Omega 2022, 7, 13075−13082

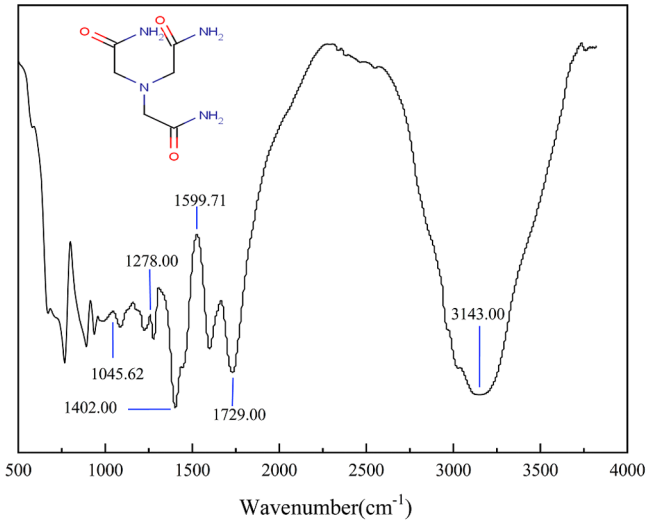

Figure 5. IR spectra of NTA.

recorded in the range of 1599.71−1045.62 cm^{-1} were due to the stretching vibration of C−N in amide. Based on these results, it can be concluded that the designated target product was successfully synthesized. Figure 6 shows the H-NMR

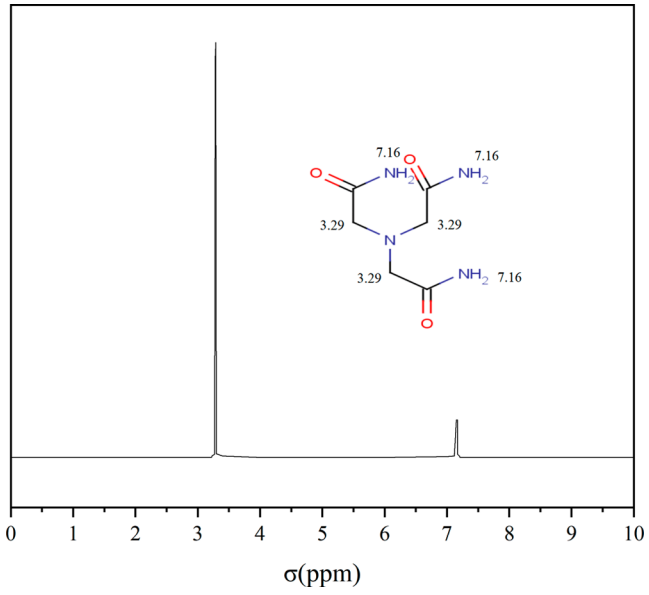

Figure 6. H-NMR spectra of NTA.

spectra of ammonia triacetamide. It can be noticed that there are types of hydrogen atoms with respect to the chemical environment. On the one hand, there are six hydrogen atoms on three amino groups showing a chemical shift of 7.16 ppm, while on the other hand, six hydrogen atoms on three carbon−carbon bonds appear at 3.29 ppm.

3.1.2. TGA of NTA. The TGA curve of the scale inhibitor recorded from ambient temperature to 600 °C in a N_2 atmosphere is presented in Figure 7. The first region between 25 and 125 °C with a small loss was due to the evaporation of water molecules and CA. The second region between 125 and 190 °C with a large slope was attributed to the decomposition of amino functional groups in the scale inhibitor. The slight deceases observed between 190 and 270 °C could be correlated with the decomposition of amide functional groups

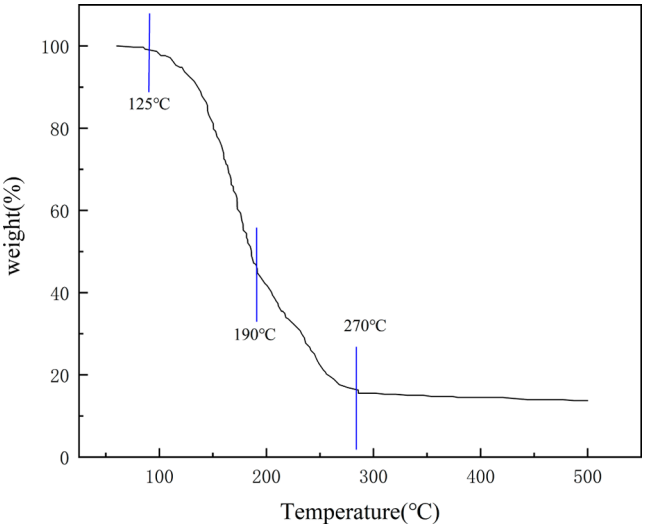

Figure 7. TGA curves of NTA.

in unreacted CA. In the light of these results, it can be seen that the threshold stability of the product was at 125 °C, which is higher than the formation temperature, suggesting its suitability to act as a salt inhibitor under hostile conditions.

3.1.3. Microstructure of Ammonia Triacetamide Salt Inhibition. The microscopic structures of sodium chloride crystals in the presence of NTA and without the salt inhibitor were observed using a biological microscope, as indicated in Figure 8. As depicted in Figure 8a, the sodium chloride crystals

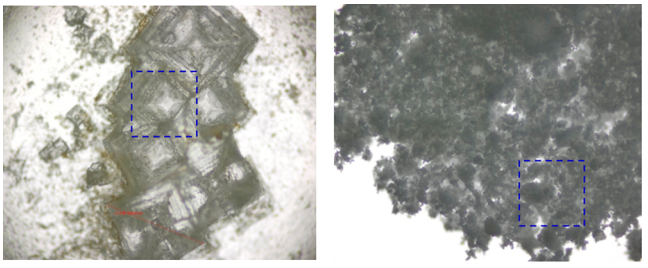

Figure 8. Microstructure of salt crystallization: (a) without and (b) with an ammonia triacetamide inhibitor (×200).

without the scale inhibitor had a regular cubic shape while those added with NTA were snowflake-like loose crystals which could be readily washed out by the formation of water, leading to favorable obstruction of the formation of salt-like cards. This was ascribed to the uniform distribution of nitrogen atoms in NTA around the Na^+ ions. Simultaneously, the significant steric hindrance effect arising from the three acetamide groups led to repulsion of the Na^+ and Cl^- ions from the inward solution, as a result not only opposing the crystal growth but also their packing.

3.2. Evaluation of the Salt Inhibition Effect of the Antisalt Composite. The experimental signature of desalinization ratio with respect to the antisalt composite concentration at room temperature is presented in Figure 9. It can be seen that as the concentration of the antisalt composite increased from 0.5 to 1.2%, the rate of desalinization reached an optimal value of 95.6%, which corresponded to a dissolution rate of 12.33%, suggesting that the composite had reached the equilibrium. Continuing the increase of the antisalt composite

https://doi.org/10.1021/acsomega.2c00452
ACS Omega 2022, 7, 13075−13082

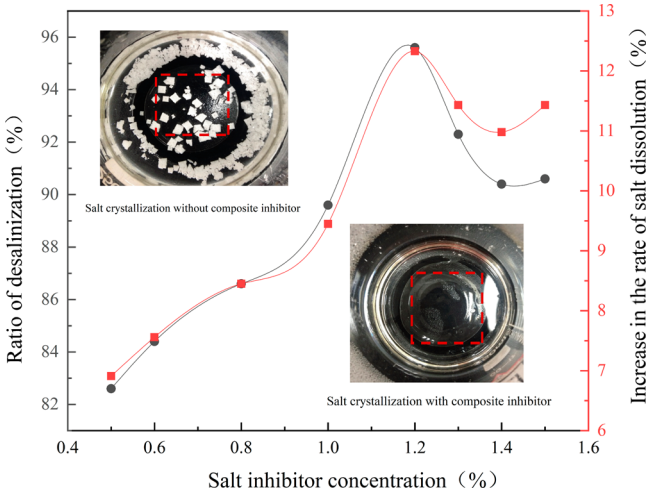

Figure 9. Effect of the salt inhibitor concentration on the antisalt effect (composite salt inhibitor: 70% NTA+ 20% SDBS +10 %PASP).

compromised the inhibitory action of the composite as the equilibrium was reversed, and the antisalt composite became saturated at 1.5%. As shown in the inset of the same figure, the saturated brine solution added with a 1.2% antisalt composite clearly presented no salt crystallization after being heated to 100 °C. Comparatively, the saturated brine solution without the composite salt inhibitor showed a number of regular cubic-shaped crystals when treated under identical conditions.

3.3. Calculation of the Binding Energy between Sodium Chloride and the Salt Inhibitor. The binding energy refers to the interaction energy between sodium chloride and the salt inhibitor. The greater the binding energy between the two species, the stronger the mutual adsorption capability, promoting a sufficiently stable adsorption system.[22−24]

From the results listed in Table 1, it can be noticed that the greater the binding energy between sodium chloride and the surface of antisalt composite, the higher the susceptibility to hinder the deposition and packing of Na^+ and Cl^- ions onto the surface of the salt crystal in the solution, consequently hampering the growth rate of sodium salt crystallization. With respect to the order of binding energy, it was pleasant for us to note the inhibition energy of each unit mass of the salt inhibitors on sodium chloride crystallization as follows: SDBS > NTA > PASP.

3.4. Calculation of the Deformation Energy of the Salt Inhibitor. The combination of sodium chloride and the antisalt composite induced adsorption at the interface, causing variation in the molecular morphology of the antisalt composite. Consequently, the modification in adsorption can be characterized by the energy variation, which also refers to the deformation energy. Calculation results of the deformation energyare shown in Table 2; it can be seen that the greater the binding energy between the surface of sodium chloride and the antisalt composite, the higher the susceptibility to oppose the precipitation and packing of Na^+ and Cl^- ions onto the surface of the salt crystal in the inward solution, as a result decreasing the growth rate of sodium chloride crystallization. With reference to the order of binding energy, the inhibition energy of each unit mass of the salt inhibitors on the sodium chloride crystal could be ordered as follows: NTA > PASP > SDBS.

3.5. Radial Function of the Atomic Action of the Antisalt Composite. The radial distribution function is used to represent the density of particles including molecules, atoms, colloidal particles, and so forth with reference to the particle system in statistical mechanics. It is also referred to the distribution probability of other particles at different distances from a given particle in space relative to a given coordinate.[25−27] In this work, the strength of interaction was assimilated to the variation of the distance between the oxygen or nitrogen atoms and the sodium atom in the sodium chloride crystal. In Figure 10, it can be noticed that NTA yielded shorter distance in-between the atoms than SDBS and PASP, suggesting a greater action probability, as a result being more prone to dynamic adsorption which rendered the antisalt effect.

Generally, the dynamic adsorption taking place in the presence of SDBS and sodium chloride crystals occurs between the sodium atoms of the crystal and oxygen atoms of the hydrophilic groups that constitute SDBS while that of NTA mainly occurs between nitrogen atoms in the amino groups and oxygen atoms in the carbonyl groups. In the case of PASP, this adsorption occurs between the nitrogen atoms in the amino groups and oxygen atoms in the carbonyl groups. Having these in mind, as indicated in Figure 11, we could find that the radial function distribution of oxygen and sodium atoms which constitutes the hydrophilic moieties of SDBS reached 18% at the highest peak of 2.5 Å while that of PASP almost reached 1.8%. Comparatively, NTA exhibited no obvious frequency distribution. Nevertheless, the radial function distribution of nitrogen and sodium atoms in the amino groups reached 11% at the highest peak of 2.5 Å, while for PASP, it was only 0.6%. It is worth noting that the adsorption with NTA was stronger than that with SDBS because the adsorption mainly occurred on the nitrogen atoms, while in the latter, it took place on the oxygen atoms. Nevertheless, the oxygen and nitrogen atoms of PASP exhibit a certain adsorption with a weaker strength. Taking into consideration the microscopic of picture of NTA and the performance of the antisalt composite presented in Figures 7 and 8, respectively, it is believed that the main action of the antisalt composite was between both nitrogen atoms of the NTA structure/nitrogen atoms of the SDBS structure and Na^+ ions of the sodium chloride crystal, resulting in strong adsorption. This effect caused sodium chloride crystals to loosen from the cubic structure, and the structure surrounded by Na^+ would repel Cl^-, leading to stabilization of Na^+ and Cl^- in the supersaturated solution. Consequently, the solubility rate of sodium chloride would increase. Lastly, as PASP has a long chain structure, it can be involved in the process of

Table 1. Binding Energy between the Sodium Chloride Salt and Salt Inhibitor System

salt inhibitor	E_{total} (kcal/mol)	$E_{inhibit}$ (kcal/mol)	$E_{surface}$ (kcal/mol)	$E_{binding}$ (kcal/mol)	molecular weight of M g/mol	$EM_{binding\ energy}$ (kcal/mol)
NTA	102.70	68.90	0	43.81	188.19	0.2328
SDBS	33.80	−49.60	0	83.40	326.50	0.2554
PASP	−167.5	−356.44	0	188.94	1168.89	0.1616

https://doi.org/10.1021/acsomega.2c00452
ACS Omega 2022, 7, 13075−13082

Table 2. Binding Energy between the Sodium Chloride Salt and Salt Inhibitor System

salt inhibitor	$E_{deformation}$ kcal/mol	$E_{free\ energy}$ kcal/mol	$E_{adsorption\ energy}$ kcal/mol	molecular weight of M g/mol	$EM_{deformation}$ kcal/g
NTA	15.58	68.90	84.48	188.19	0.0828
SDBS	−52.41	−49.5	−2.91	326.50	−0.1605
PASP	92.06	−356.5	−264.44	1168.89	0.0787

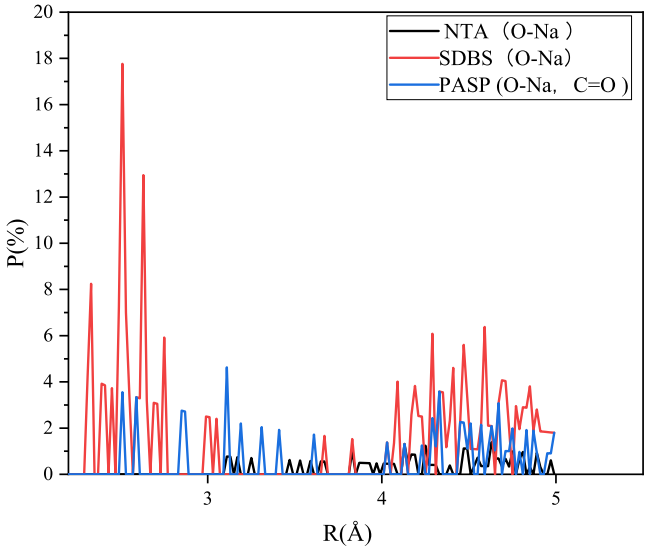

Figure 10. Relationship between the action distance and probability of the O−Na atom of the antisalt composite.

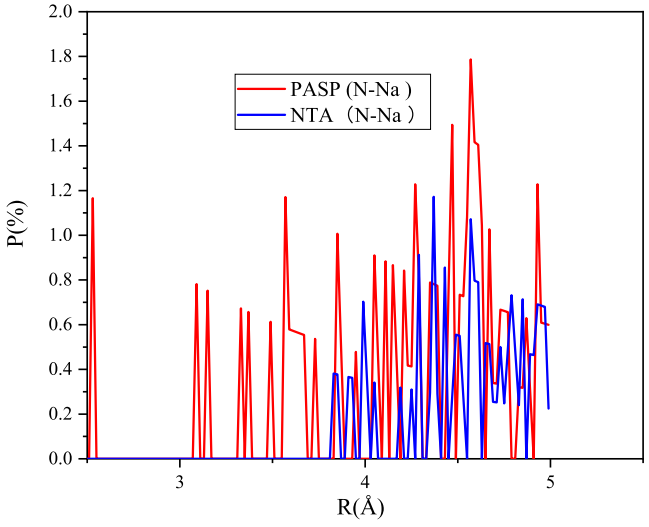

Figure 11. Relationship between the action distance and probability of the N−Na atom of the antisalt composite.

crystallization, driving certain auxiliary action and eventually improving the salt inhibition effect.

4. CONCLUSIONS

An antisalt composite composed of PASP, SDBS, and NTA, which was prepared from CA, was proposed as a high-temperature antisalt agent. It was found that the optimal concentration of the composite agent was 1.2% as the dissolution rate and inhibition rate were 95.6 and 12.33%, respectively, at a temperature of 100 °C, which resulted in alteration of the morphology of the sodium chloride crystal. The salt inhibition mechanism evidenced that the main action was between both nitrogen atoms of the NTA structure/nitrogen atoms of the SDBS structure and Na^+ ions of the sodium chloride crystal, resulting in strong adsorption. Moreover, this effect caused the sodium chloride crystals to loosen from the cubic structure, and the structure surrounded by Na^+ repelled Cl^-, resulting in stabilization of Na^+ and Cl^- in the supersaturated solution. Furthermore, PASP had a long chain structure, and it could be involved in the process of crystallization and ultimately improve the salt inhibition effect.

AUTHOR INFORMATION

Corresponding Author

Chao Ma − *School of Petroleum Engineering, Yangtze University, Wuhan 434100, China; Key Laboratory of Oil and Gas Drilling and Production Engineering, Wuhan 434100, China; Leak Resistance & Sealing Technology Research Department National Engineering Laboratory of Petroleum Drilling Technology, Wuhan 434100, China;* orcid.org/0000-0001-9736-5337; Email: 500526@yangtzeu.edu.cn

Authors

Yan Chen − *School of Petroleum Engineering, Yangtze University, Wuhan 434100, China*

Wen dong Ren − *School of Petroleum Engineering, Yangtze University, Wuhan 434100, China*

Xing yu Liu − *School of Petroleum Engineering, Yangtze University, Wuhan 434100, China*

Wen Gu − *School of Petroleum Engineering, Yangtze University, Wuhan 434100, China*

Hui li Zhou − *Wuhan Changde Energy Technology Co. Ltd., Wuhan 430100, China*

Complete contact information is available at: https://pubs.acs.org/10.1021/acsomega.2c00452

Notes

The authors declare no competing financial interest.

ACKNOWLEDGMENTS

We acknowledge the Xinjiang Autonomous Region Natural Science Fund Project—Study on Synthesis and Oil Displacement Mechanism of Porous Hyperbranched Heavy Oil Cold-Collecting and Viscosity-Release Oil Displacement Agent (2019D01A91)—and the Opening Project of State Key Laboratory of Polymer Materials Engineering (Sichuan University) (sklpme2018-4-36) for financial support.

REFERENCES

(1) Khormali, A.; Petrakov, D. G.; Faculty, O. G. Laboratory investigation of a new scale inhibitor for preventing calcium carbonate precipitation in oil reservoirs and production equipment. *Pet. Sci.* **2016**, *13*, 320−327.

(2) Jin, H. P. *Saltification mechanism and development technology of high salinity oilfield*; China University of Geosciences: Beijing, China, 2011.

(3) Han, L. Research and application of salt prevention technology for inter-salt argillaceous dolomite reservoirs. *J. Jianghan Pet. Power Univ.* **2017**, *30*, 38−54.
(4) Ma, C.; Li, L.; Xiao, J.; Zhang, X. Salt inhibition effect of compound salt inhibitor in high salt formation water. *Sci. Technol. Eng.* **2016**, *16*, 143−147.
(5) Wu, Z. X. *Cause analysis and plugging removal measures of surface gathering and transportation system in Wuzhixin Puguang Gas Field*; China University of Petroleum (East China): Qingdao: Shandong, China, 2012.
(6) Ma, C.; Li, L.; Xiao, J.; Zhang, X. Study on the law of water and salt deposition in interlayer strata of Wangchang Oilfield. *Sci. Technol. Eng.* **2015**, *15*, 65−169.
(7) Gong, B. Study on water injection huff and puff technology of salt shale reservoir. *J. Jianghan Pet. Worker's Univ.* **2019**, *32*, 28−30.
(8) Yan, F. Research on compound salt inhibitor and its application in Yingxi Oilfield. *Special Reservoirs* **2019**, *26*, 142−146.
(9) Liu, J. S. *Research and application of salt removal and prevention technology for oil wells*; China University of Petroleum (East China): Qingdao: Shandong, China, 2014.
(10) Yao, S. Z.; Xiong, W. L.; Lei, J. J. Salting mechanism and prevention measures of wen 96 underground gas storage. *Nat Gas Technl. Econ.* **2021**, *15*, 32−37.
(11) Zhang, W. F.; Lin, X. M.; Jiang, L. X.; Wang, Z. G. The promotion and application of wellbore-formation integrated salt control plugging removal technology in Wenliu Oilfield. *Chem. Des. Commun.* **2017**, *43*, 58−73.
(12) Jiang, Z.; Shen, W. D.; Ma, C.; Cai, Z. M.; Ma, L.; Tang, S.; He, C. H.; Xu, M.; Zhou, Q. The application of composite salt inhibitor desalting and plugging removal technology in gas pipelines. *Nat. Sci.* **2020**, *4*, 233−238.
(13) Chen, H. J.; Ma, X. L.; Guo, C. J.; Gao, C. Q.; Yang, H. Y. The application of comprehensive salt suppression and plugging removal technology in Zhongyuan low permeability oilfield. *Petrol. Chem. Appl.* **2014**, *33*, 25−27.
(14) Liu, Y. *Research on a salt and scale inhibitor for oilfield*; Southwest Petroleum: Chengdou, Sichuan, China, 2014.
(15) Li, H. B.; Li, X.; Nie, Y.; Wu, B. Z. Study on Indoor Experiment of DXGYZ-1 in Oil Well. *China Pet. Chem. Stand. Qual.* **2012**, *268*, 53.
(16) Rodriguez-Navarro, C.; Linares-Fernandez, L.; Doehne, E. Effects of ferrocyanide ions on NaCl crystallization in porous stone. *J. Cryst. Growth* **2002**, *243*, 503−516.
(17) Caine, D. M.; Paternoster, I. L.; Sedehizadeh, S.; Shapland, P. Sequential acetic acid−sodium chloride treatment to control salt stoichiometry of a hydrochloride salt. *Org. Process Res. Dev.* **2012**, *16*, 518−523.
(18) Liu, R. Z.; Zhang, B. J.; Mao, L. H. Crystallization inhibition of potassium ferrocyanide on sodium chloride. *J. Jinan Univ.* **2015**, *36*, 449−452.
(19) Zheng, R. Z.; Zhang, G. Z. Salt recrystallization inhibitor NTA. *Oilfield Chem.* **1991**, *8*, 103−107.
(20) Zhang, C. Research on scaling law and prevention technology of weak alkali compound flooding in Block Jing 11 of Zhangchao. *Huabei Oilfield*; China University of Petroleum (East China): Qingdao, Shandong, China, 2015.
(21) Tang, Y.; Zhang, F.; Cao, Z.; Jing, W.; Chen, Y. Crystallization of $CaCO_3$ in the presence of sulfate and additives: Experimental and molecular dynamics simulation studies. *J. Colloid Interface Sci.* **2012**, *377*, 430−437.
(22) Luo, P.; Zhai, Y.; Senses, E.; Mamontov, E.; Xu, G.; Z, Y.; Faraone, A. Influence of kosmotrope and chaotrope salts on water structural relaxation. *J. Phys. Chem. Lett.* **2020**, *11*, 8970.
(23) Zheng, R. Z.; Zhang, G. Z. Salt recrystallization inhibitor NTA. *Oilfield Chem.* **1991**, *8*, 103−107.
(24) Qi, S. T.; Che, T. H.; Tan, X.; Liu, G. Q. Research progress of salt inhibitors for tight sandstone gas wells. *Appl. Chem. Eng.* **2019**, *48*, 2231−2234.
(25) Zhuang, C. Q.; Yue, H.; Zhang, H. Application of molecular simulation method and simulation software Ma-materials Studio in polymer materials. *Lastics* **2010**, *39*, 81−84.
(26) Tang, Y.; Zhang, F.; Jing, W.; Chen, Y.; Chen, Y. Crystallization of $CaCO_3$ in the presence of sulfate and additives: Experimental and molecular dynamics simulation studies. *J. Colloid Interface Sci.* **2012**, *377*, 430−437.
(27) Yu, J. L.; Wang, Z. K.; Huo, R.; Cui, Y. J.; Sun, Q. Q.; Hu, S. Q. The scale inhibition performance and scale inhibition mechanism of calcium carbonate scale inhibitor in weak alkali environment. *Oilfield Chem.* **2017**, *34*, 699−704.

https://doi.org/10.1021/acsomega.2c00452
ACS Omega 2022, 7, 13075−13082